



High Enthalpy Effects on Hypersonic Boundary-Layer Transition: T5 Experimental and Numerical Comparison

A. Hameed^{*}, J. H. Chen[†], and N. J. Parziale[‡]
Stevens Institute of Technology, Hoboken, NJ 07030, USA.

J. Kuehl[§] and T. Liang[¶] and K. Graziose^{||}
University of Delaware, Newark, DE 19716, USA.

Christoph Brehm,^{**} and Sean David Dungan,^{††}
University of Maryland, College Park, MD, 20742, USA

Jean-Philippe Brazier^{‡‡}
ONERA/DMPE, Toulouse University, F-31055 Toulouse, France

L. Paquin,^{§§}
U.S. Naval Research Laboratory, Washington, DC 20375, USA

S. J. Laurence^{¶¶}
University of Maryland, College Park, MD 20742, USA

In this paper, a numerical and experimental comparison is presented of a slightly blunted, 5° half-angle cone at high-enthalpy flow conditions. Experimental studies were conducted at California Institute of Technology’s T5 free piston reflected shock tunnel. Numerical stability investigations were conducted with STABL, MAMOUT of ONERA, JoKHeR of the University of Delaware, and CHAMPS of the University of Maryland. The comparison focuses on second-mode instability physics at high-enthalpy. The NLDE based solver was most accurate at identifying the most amplified frequency, however, significant uncertainty was observed in both N factor maximum amplitude and most amplified frequency amongst the various stability solvers. A comparison of solver results between experiments performed with an isothermal wall and an actively-cooled wall shows various degrees of success in portraying sensitivity to wall temperature.

^{*}Graduate Student, Mechanical Engineering, 1 Castle Point on Hudson, Hoboken, New Jersey, 07030, USA.

[†]Graduate Student, Mechanical Engineering, 1 Castle Point on Hudson, Hoboken, New Jersey, 07030, USA.

[‡]Associate Professor, Mechanical Engineering, 1 Castle Point on Hudson, Hoboken, New Jersey, 07030, AIAA Associate Fellow.

[§]Associate Professor, Mechanical Engineering, 130 Academy Street, Newark, Delaware 19716, USA.

[¶]Graduate Student, Mechanical Engineering, 130 Academy Street, Newark, Delaware 19716, USA., AIAA Student Member.

^{||}Graduate Student, Mechanical Engineering, 130 Academy Street, Newark, Delaware 19716, USA., AIAA Student Member.

^{**}Associate Professor, Aerospace Engineering, 3179 Glenn L. Martin Hall Bldg, cbrehm1@umd.edu. Member AIAA

^{††}Graduate Research Assistant, Aerospace Engineering, 3179 Glenn L. Martin Bldg, sdungan@umd.edu. Student Member AIAA

^{‡‡}Research Scientist, ONERA DMPE, Toulouse, France, Jean-Philippe.Brazier@onera.fr

^{§§}Aerospace Engineer, Naval Center for Space Technology, U.S. Naval Research Laboratory, Washington, DC 20375, AIAA Member.

^{¶¶}Associate Professor, Aerospace Engineering, Department of Aerospace Engineering, College Park, Maryland, 20742. Senior AIAA Member.

Distribution Statement A: Approved for public release. Distribution unlimited.

I. Introduction

Understanding the process of boundary-layer transition at flight-relevant enthalpy is important in hypersonic vehicle design. Following the onset of boundary-layer transition, there is a drastic increase in aeroheating and viscous shear stress experienced by the vehicle. During tests of ballistic reentry vehicles, the surface heating rate was found to have increased by a factor of 5 downstream of the transition location [1]. For slender bodies, the heating rate increased by a factor of 3 following transition of the laminar boundary layer [2]. Additionally, there remains considerable uncertainty in predicting the location of boundary-layer transition. Reviewers noted a 60% error in estimating the location of transition along the body of the National Aerospace Plane [3] and Schneider’s review of hypersonic flight data [1] found a 300% uncertainty in transition location prediction. The substantial increase in aeroheating and the large degree of uncertainty associated in predicting the transition location suggests the process of hypersonic boundary-layer transition is relevant but not well understood.

At the high enthalpies experienced during hypersonic flight, the temperature at the boundary-layer edge (T_E) is greater than the temperature of the vehicle’s wall (T_W). In his analysis of Sherman and Nakamura’s [4] re-entry flight data for a 22° half-angle blunt cone at Mach 6, Malik [5] computed a post-shock temperature of 3300 K, giving a wall-to-edge temperature ratio (T_W/T_E) of 0.22. Studies have shown the lower wall-to-edge temperature ratio destabilizes Mack’s second-mode instability [6–8]. Through a chemical equilibrium, thermal nonequilibrium LST analysis, Bitter and Shepherd [9] found that decreasing the wall-to-edge temperature ratio to values more representative of conditions in high-enthalpy facilities doubled the maximum second-mode N factor. The high level of wall-cooling was also found to produce unique boundary-layer features. In addition to the near-wall sonic line, which acts as a wave guide and traps the acoustic disturbance waves, when the disturbance phase speed is slow enough, a second supersonic region emerges above the critical layer, with its own relative sonic line [10]. In this region, the disturbance phase speed travels supersonically upstream with respect to the freestream. The solution to the boundary layer stability equations is wave-like in this region, and the decaying acoustic waves emanating out of the boundary layer are slanted at approximately the Mach wave angle. Bitter and Shepherd’s analysis at cooled-wall conditions suggested these supersonic unstable modes caused the second-mode instability to remain unstable over a broader range of frequencies [9]. Knisely and Zhong further investigated the supersonic mode over a highly-cooled (case 1: $T_W/T_E = 0.2$, case 2: $T_W/T_E = 0.667$), 5° blunt cone using linear stability theory (LST) [10] and direct numerical simulation (DNS) [11]. Their work confirmed the existence of the supersonic mode using both DNS and LST for case 1, but they were able to resolve the weak supersonic mode at the higher temperature ratio only using DNS. They also confirmed the destabilizing effects of the cooled wall on the supersonic mode [9, 12]. Chuvakhov and Fedorov [12] suggested that the supersonic mode may have stabilizing effects on the second-mode instability by radiating energy away from the boundary layer. Unnikrishnan and Gaitonde [13] investigated the effect of a cooled wall on a Mach 6 boundary layer using a sequence of LST, nonlinear two-dimensional and three-dimensional DNS. While the cooled wall increased the spontaneous radiation of the acoustic waves out of the boundary layer, they found the destabilizing effect of the lower wall-to-edge temperature ratio was much stronger and did not observe an attenuation of the second-mode instability.

Additional studies performed at high levels of wall-cooling have focused on the effects of chemical reactions. Using parabolized stability equations (PSE) to analyze Mach 20 flow over a sharp, 6° wedge, Chang et al. [14] estimated the transition onset to be at 14 ft for an equilibrium gas model and 39 ft for a perfect gas model, highlighting the importance of accounting for flow chemistry at high enthalpy. Using computational fluid dynamics and linear stability theory, Johnson et al. [15] reproduced the conditions of shock tunnel experiments performed by Adam and Hornung [16] and Germain and Hornung [17] at California Institute of Technology’s free piston shock tunnel, T5. The computational trends agreed with the experimental observations; the transition Reynolds number increased with increasing free-stream total enthalpy, with the rate of increase being greater for gases with lower dissociation energies. Generally, chemical reactions were found to produce a more unstable boundary layer. However, the introduction of chemistry was found to stabilize or destabilize the boundary layer depending on the endothermic or exothermic nature of the reaction, with exothermic reactions having higher disturbance amplification rates. Malik [5] confirmed the destabilizing nature of chemistry in his analysis of high-Mach-number transition data using a reacting flow parabolized stability equations code. Despite the large discrepancy in edge conditions and transition Reynolds numbers between the two cases analyzed, the N factors at the experimentally observed transition onset locations were remarkably similar and compared well with results from hypersonic flight experiments and quiet tunnels.

Due to the practical and physics-related challenges inherent to high-enthalpy ground-test facilities, namely, high cost of construction and operation, short test duration, flow quality, and particulate contamination, few experimental investigations have been performed at flight-relevant enthalpies. Vidal and Golian [18] investigated the heat transferred to catalytic and non-catalytic surfaces on a sharp flat plate in a shock tube at $T_W/T_E = 0.09$. East et al. [19] measured

heat-transfer rates over a flat plate in the T3 free piston reflected shock tunnel at stagnation enthalpies from 2 MJ/kg to 51 MJ/kg. Germain [20] performed an exploratory study at T5 using a 5° half-angle cone and found real-gas effects stabilized the boundary layer. Adam's [21] studies at T5 reinforced Germain's [20] earlier results, noting that the transition Reynolds number increased with increasing reservoir enthalpy. Additional boundary-layer transition and stability research in T5 was performed to dampen the acoustic instability [22, 23], quantify the role of energy exchange between the boundary-layer instability and the fluid [24], and increase the transition Reynolds number of a test gas by seeding its boundary layer with a gas to dampen the acoustic instability [25–29]. Parziale et al. [30, 31, 32] and Parziale [33] used a novel, non-intrusive, optical flow-diagnostic technique called focused laser differential interferometry (FLDI) at T5 to track the evolution of the second-mode instability along the model. Knowing the spacing between the FLDI detectors and the time at which the signal was registered by each probe, Parziale et al. were able to determine the group velocity of the narrowband second-mode disturbance to be nearly equal to the edge velocity of the boundary layer. Additional high-enthalpy experimental campaigns have been performed in shock tunnels around the world. In JAXA's HIEST facility, Tanno et al. [34, 35] performed experiments at stagnation enthalpies up to 18 MJ/kg. They used surface-mounted thermocouples to determine the transition Reynolds number over a 7° half-angle cone and were able to measure the second-mode instability using pressure transducers up to $h_0 = 12$ MJ/kg. Laurence et al. [36] performed low-enthalpy experiments ($h_0 = 3.1$ -3.3 MJ/kg) and a single high-enthalpy experiment ($h_0 = 11.9$ MJ/kg) at DLR's HEG facility. They observed the nature of the wavepacket differed depending on the enthalpy, with the disturbance energy more closely concentrated near the wall for the high-enthalpy condition.

In this work, results from experiments performed by Hameed et al. [37, 38] and Paquin et al. [39] at the T5 free piston reflected shock tunnel are compared to numerical stability computations conducted using STABL of VirtusAero, MAMOUT of ONERA, JoKHeR of the University of Delaware, and CHAMPS of the University of Maryland to analyze the physics of the second-mode instability at high-enthalpy and the role of real-gas effects. The selected experiments featured varying conditions, highly cooled boundary layers with active wall-cooling in some cases, and a blunt cone nose tip.

II. Facility and Experimental Setup

A. T5 Reflected Shock Tunnel

The experiments in this campaign were performed at California Institute of Technology's T5 free piston reflected shock tunnel. T5 is capable of producing flows up to specific reservoir enthalpy of 25 MJ/kg, reservoir pressure of 100 MPa, and reservoir temperature of 10,000 K. By generating high enthalpy flows at high density, this facility simulates the chemical nonequilibrium effects of vehicles flying at hypervelocity speeds through the atmosphere. Additional information regarding the capabilities of T5 can be found in Hornung [40].

T5 is separated into four sections: secondary reservoir, compression tube, shock tube, and test section. In preparation for an experiment, a thick steel primary diaphragm is installed at the shock tube/compression tube junction, a thin mylar secondary diaphragm is placed between the test section and the shock tube, and a 120 kg piston is loaded in the launch manifold between the secondary reservoir and the compression tube. Next, each section of the facility is independently evacuated to an acceptable level of vacuum. The shock tube is then filled with the test gas (ALPHAGAZ™ air for these experiments), the compression tube is filled with a Helium/Argon mixture, and the secondary reservoir is pressurized with air. The piston is launched down the compression tube when the pressurized air in the secondary reservoir is allowed to push against the back of the piston. The accelerating piston adiabatically compresses the driver gas in the compression tube until the primary diaphragm is ruptured. The rupture of the primary diaphragm causes a shock wave to propagate into the shock tube, which reflects off the end wall, bursts the secondary diaphragm, and re-processes the test gas to the nozzle reservoir conditions. The test gas is then expanded through the converging-diverging contoured nozzle to a hypersonic Mach number (typically $M \approx 5.2$) in the test section.

B. Test Model

A 5° half-angle cone with a slightly-blunted interchangeable nose tip ($R_N = 2$) was used as the model in this experimental campaign. The cone was placed at approximately 0° angle of attack in the spanwise center of the test section. Shot 2990 used a cone with no interior cooling capabilities. For shots 3019, 3022, and 3026, an actively-cooled cone was manufactured to the same exterior dimensions as the original model. The actively-cooled cone was machined in two halves and featured an internal cavity to house a cooling coil. The cooling coil extended approximately halfway

into the cone and liquid nitrogen (LN_2) entered and exited the coil from the rear of the cone in a single-pass configuration. A solid copper heat exchanger was used to conduct the cooling from the cooling coil to the cone's nose tip. De-icer was applied to the cone's surface to reduce the risk of frost developing during the cooling process. To measure the cone's surface temperature distribution prior to the experiment, the cone was instrumented with type K thermocouples internally routed toward the cone's surface and located at various circumferential positions throughout the length of the cone. A model of the actively-cooled cone is presented in Fig. 1.

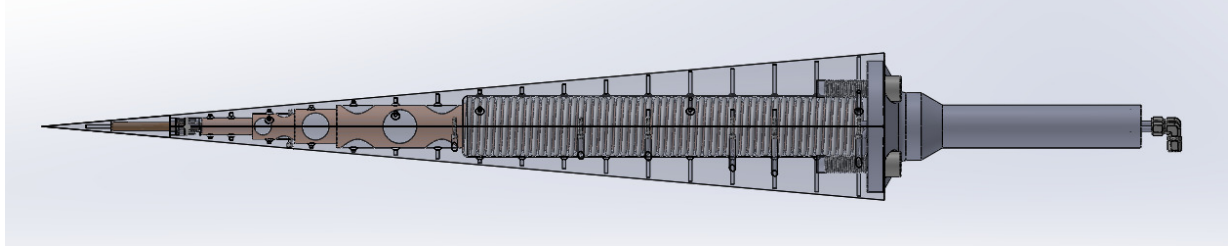


Fig. 1 Model of the actively-cooled cone used for shots 3019, 3022, 3026 showing the cooling coil, copper heat exchanger, and thermocouple ports.

C. Calculation of Run Conditions

The nozzle reservoir conditions are used to estimate the freestream run conditions. The thermodynamic state of the test gas in the nozzle reservoir is determined using the shock tube pressure, P_1 , and the measured incident shock speed, U_s . Using Cantera[41] with the Shock and Detonation Toolbox[42], we assume isentropic expansion of this state to the reservoir pressure, P_R , accounting for weak expansion or compression waves that are reflected between the contact surface and the shock tube end wall. The calculated nozzle reservoir conditions are inputted into the University of Minnesota Nozzle Code to determine the freestream conditions at the exit of the contoured nozzle [43–46]. The reservoir and freestream conditions for the shots discussed in this paper are presented in Table 1 and Table 2. The freestream conditions are chosen to be an areal average of the DPLR output at approximately 580 ± 10 mm, the distance from the nozzle's throat to the location of the model's nose tip. The temperature profile along the cone is shown in Table 3. Shot 2990 featured an isothermal wall. The wall temperature profile varied for shots 3019, 3022, and 3026, and was specified based on thermocouple measurements taken prior to the run.

Table 1 Reservoir Conditions

Shot	Gas	P_R (MPa)	h_R (MJ/kg)	T_R (K)	ρ_R (kg/m ³)	y_{N_2} (-)	y_{O_2} (-)	y_{NO} (-)	y_{N} (-)	y_{O} (-)	R_N (mm)	Diag (-)
2990	Air	59.6	8.86	5727	33.3	0.699	0.068	0.141	0.003	0.090	2	FLDI
3019	Air	61.6	9.67	6076	31.9	0.698	0.052	0.137	0.005	0.108	2	Schlieren
3022	Air	62.0	9.43	5976	32.8	0.698	0.057	0.139	0.004	0.102	2	FLDI
3026	Air	62.2	9.19	5875	33.7	0.698	0.061	0.140	0.003	0.097	2	FLDI

D. FLDI Setup

The components used to generate the FLDI diagnostic employed in the experimental campaign are shown in Fig. 2. The 532 nm linearly-polarized beam output of a Cobolt 05-01 laser was first expanded using a diverging lens. The diverging beam was then passed through two diffractive optics (Holo/Or MS-474-Q-Y-A and DS-192-Q-Y-A) to generate a grid, which was circularly polarized using a quarter-wave plate. Each beam in the grid was split once more into orthogonally polarized beam pairs using a 2 arcminute Wollaston prism. Next, the beams passed through a converging lens and then entered the test section. The position of the diverging lens was adjusted relative to the upbeam converging lens (left C_2 in Fig. 2) to locate the focus of the beams at the top-center of the cone. The lowest row of beams was positioned at a height equal to approximately half of the boundary-layer thickness above the cone. Downbeam of the test section, the diverging FLDI beam pairs were focused using a converging lens and then recombined using a Wollaston

Table 2 Freestream Conditions

Shot	U_X	ρ_X	P_X	T_X	T_{vX}	M_X	Re_X^U	y_{N_2}	y_{O_2}	y_{NO}	y_N	y_O
	(m/s)	(kg/m ³)	(kPa)	(K)	(K)	(-)	(1/m)	(-)	(-)	(-)	(-)	(-)
2990	3809	0.087	34.2	1355	1363	5.13	6.35e+06	0.733	0.187	0.073	0.000	0.007
3019	3953	0.085	37.3	1511	1518	5.03	5.99e+06	0.733	0.184	0.073	0.000	0.010
3022	3912	0.087	37.0	1466	1473	5.06	6.18e+06	0.733	0.185	0.073	0.000	0.009
3026	3870	0.089	36.5	1419	1427	5.09	6.38e+06	0.733	0.186	0.073	0.000	0.008

Table 3 Temperature Distribution on Cone Surface

Shot	Distance Along Cone (m)														
	0.000	0.073	0.118	0.218	0.268	0.318	0.368	0.418	0.468	0.518	0.568	0.618	0.668	0.718	0.818
Shot	Temperature (K)														
2990	293.2	293.2	293.2	293.2	293.2	293.2	293.2	293.2	293.2	293.2	293.2	293.2	293.2	293.2	293.2
3019	249.1	242.1	239.5	238.7	236.4	233.9	241.6	248.2	252.9	256.2	259.8	262.3	264.2	266.3	270.2
3022	257.6	255.8	255.8	256.2	256.6	257.6	258.6	262.1	264.4	266.6	269.0	271.4	273.2	274.8	278.3
3026	258.2	253.0	250.1	249.8	245.9	241.7	244.9	250.8	253.1	259.4	263.8	267.2	269.5	272.1	275.2

prism of an equivalent separation angle. Finally, the grid of beams was passed through a linear polarizer and each beam was directed onto an individual photodetector using an array of lenses.

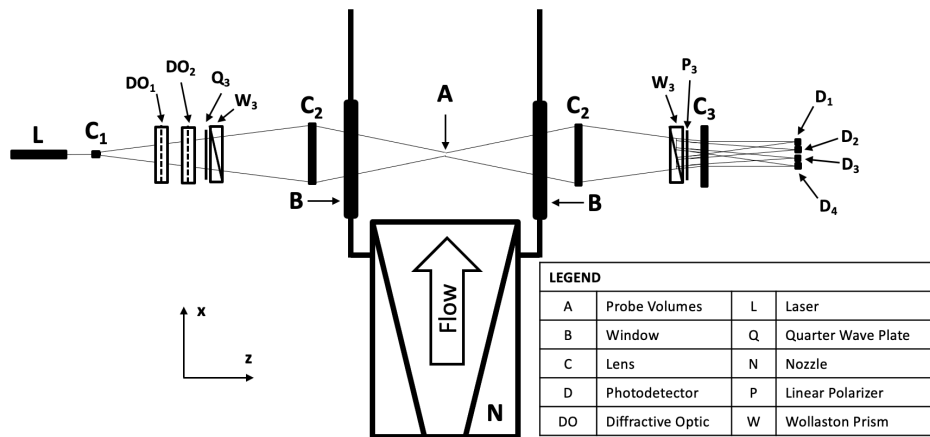


Fig. 2 Optical components used to generate the FLDI diagnostic in this experimental campaign. The diffractive optics generated a grid of beams interspaced in the streamwise and wall-normal direction. The Wollaston prism generated beam pairs intraspaced in the streamwise direction.

The FLDI beam pairs used to probe the flow in shot 2990 are shown in Fig. 3. In this experiment, the flow was interrogated using the lowest row and upstream column of beam pairs. This selection positioned two beam pairs within the boundary layer (FLDI probes C and D) and two beam pairs at various heights above the boundary layer (FLDI probes A and B). The boundary layer, shown as the dashed line in Fig. 3, was determined to be approximately 1 mm thick at the measurement location of 680 mm along the cone. The velocity profile at this position is represented as a solid white line. Both the boundary-layer thickness and the velocity profile were determined using DPLR. A similar configuration of the FLDI beams was used for shots 3022 and 3026. However, in these experiments, the lowest row and the downstream column of beam pairs was used to examine the flow. Additionally, there were minor differences in the beam inter and intraspacing.

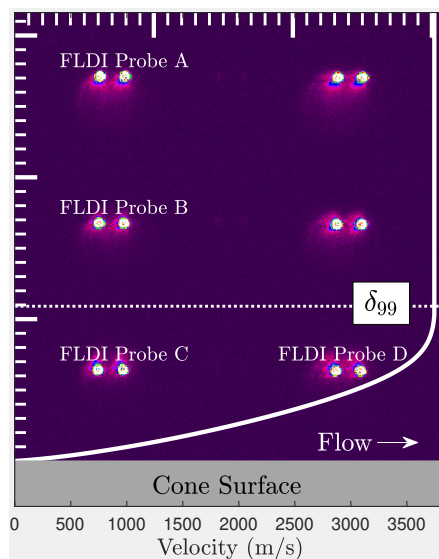


Fig. 3 Relative wall-normal and streamwise position and spacing of FLDI beam pairs for shot 2990. The major tick marks are spaced 1 mm apart and the minor tick marks are spaced 0.1 mm apart. The lowest row of beams are located approximately 0.635 mm above the cone surface. The velocity profile is given by the solid white line and the estimated boundary-layer thickness is depicted by the dotted line. The flow is from left to right.

E. Schlieren Setup

The schlieren setup explained by Paquin et al. [47] was used in shot 3019. A Cavilux HF laser was used as the light source, with an adjustable iris diaphragm to limit the amount of light to avoid image saturation. The beam was expanded using a plano-convex lens, collimated by a parabolic mirror, and directed through the test section using multiple planar mirrors. Downbeam of the test section, another parabolic mirror focused the beam to a point, where the knife edge was inserted. The beam was next passed through a bandpass filter to minimize test-gas luminosity from obscuring the image and a series of plano-convex lenses were used to increase the magnification of the image. The images were collected by a high-speed camera at a frame rate of 666 kHz with a resolution of 1280 x 64 pixels, providing a spatial scale of 0.13 mm/pixel. The field of view was approximately 17 cm in the streamwise direction and 7 cm in the wall-normal direction, located approximately 59 cm from the nosetip.

III. Numerical Methods

A. Basic State Solver

Steady basic states flow solutions were calculated using US3D. Our hypersonic CFD process consists of: creating the geometry in Solidworks, meshing in Pointwise, running US3D to produce the steady state solutions (basic states), and visualizing the flow field in Tecplot. The wall normal data of the basic state was extracted using a combination of Tecplot and in-house developed scripts. The mesh dimensions are as follows, 1600 streamwise points, one degree rotation in the azimuthal direction (corresponds to one cell width), and test-driven convergence to determined the number of wall normal points. The flow conditions are representative of the California Institute of Technology's T5 free-piston-driven reflected-shock tunnel conditions given above.

In US3D, the inputs and boundary conditions for the freestream and the isothermal wall were calculated by using the isentropic flow relations and unit Reynolds number. The inflow conditions and wall temperature are listed in table the above tables. The other boundary conditions were defined as an outflow at the downstream end of the domain, and symmetry conditions on both azimuthal sides. Additional settings included non-reacting, laminar, viscous flow. Using CFL ramping, the calculation was run until converged, and a steady state solution was reached (Reed et al. 2014).

B. Stability tools

1. ONERA

ONERA’s local linear stability code MAMOUT is designed to compute the eigenmodes of boundary-layer profiles, assuming a slow variation of the base flow in both streamwise and crosswise directions and a fast variation along the wall normal coordinate. The Navier-Stokes equations are linearized around a given laminar base flow. The generalized eigenvalue problem is then discretized using high-order quasi-spectral compact finite-difference scheme. Incompressible fluids or perfect gas flows can be addressed, as well as a reacting mixture in chemical equilibrium, described by a Mollier chart. For a prescribed frequency, the program provides the local wave number and growth rate of the unstable wave and the associated eigenfunctions. A given mode can be tracked automatically on a prescribed frequency range for a series of boundary-layer profiles and the amplification coefficient (N factor) is then integrated.

2. JoKHeR

The JoKHeR Parabolized Stability Equations (PSE) package [48–50] was developed in collaboration with Dr. Helen Reed at Texas A&M as part of the efforts of the National Center for Hypersonic Laminar-Turbulent Transition Research. The code employs a Quasi-3D, compressible, ideal gas, primitive variable formulation; that is, it marches disturbances along a predefined path with the assumption of uniformity in the perpendicular direction. The package consists of Linear Stability Theory (LST), Linear Parabolized Stability Equations (LPSE) and Nonlinear Parabolized Stability Equations (NPSE) codes. These codes has been extensively validated against experimental [51–53] and numerical [54–56] datasets. A unique feature of JoKHeR is that it employs a nonlinear wave packet formulation for NPSE implementation which allows for the modeling of finite bandwidth disturbances [49, 57] and thus accounts for spectral broadening and low-frequency content generation [58] which is important for accurate prediction of nonlinear energy exchange [59].

3. STABL

Stability calculations for these experiments were performed using the STABL software package [15, 45]. STABL uses a two-dimensional/axisymmetric mean flow solver based on NASA’s implicit data-parallel lower-upper relaxation (DPLR) method [60]. The STABL DPLR solver uses an extended set of the Navier-Stokes equations with a two-temperature model to characterize the translational, rotational, and vibrational modes. Additional details, including the governing equations used by the mean flow solver, can be found in Johnson [45] and Johnson and Candler [61]. The stability analysis of the flow was performed using PSE-Chem, the parabolized stability equation (PSE) solver within STABL. PSE-Chem was also used to solve the linear stability theory (LST) equations, which it does by making the “locally-parallel” assumption that the mean flow only varies in the body-normal direction. PSE-Chem solves the linear parabolized stability equations derived from the axisymmetric Navier-Stokes equations [61].

Linear Stability Theory: LST considers a steady basic flow state, determined from separate CFD simulations, and solves the disturbance equation (which follows from substitution of equation 1 into the Navier-Stokes equations) assuming linear, parallel flow. The disturbance is assumed to be of the form indicated by equation 2, substitution of which into the disturbance equations leads to the generalized eigenvalue problem with α and ω being the streamwise wave number and the frequency respectively. The resulting eigenvalues are used to determine instability and the corresponding eigenvector represent the shape of the disturbance in the wall normal direction.

$$\phi(x, y, z, t) = \underbrace{\bar{\phi}(y)}_{\text{basic state}} + \underbrace{\phi'(x, y, z, t)}_{\text{disturbance}} \quad (1)$$

$$\phi' = \hat{\phi}(y)e^{i(\alpha x + \beta z - \omega t)} \quad (2)$$

Parabolized Stability Equations: Originally identified by Herbert and Bertolotti [62], during a critical review of Gaster’s [63] early nonparallel work, the parabolized stability equations have been developed as an efficient and powerful tool for studying the stability of advection-dominated laminar flows. Excellent introductions to the PSE method and summary of its early development were provided by Herbert [64]. During the early stages of both linear and nonlinear development of this technique, much was established related to basic marching procedures, curvature, normalization

conditions, and numerical stability of the method itself [65, 66]. In a relatively short time, the field rapidly expanded to include complex geometries, compressible flow, and finite-rate thermodynamics.

PSE is similar to the Fourier/Laplace transform in that it considers an initial-value problem. However, the slowly varying basic state assumption is made in the streamwise direction and a slow variable $\bar{x} = \frac{x}{Re}$ is introduced. Ultimately, disturbances are assumed of the form

$$F[\phi'] = \underbrace{\tilde{\phi}(\bar{x}, y)}_{\text{shape}} \underbrace{\Phi(x, t)}_{\text{wave}}$$

where the wave part satisfies

$$\frac{\partial \Phi}{\partial x} = i\alpha(\bar{x})\Phi \quad (3)$$

$$\frac{\partial \Phi}{\partial t} = -i\omega\Phi, \quad (4)$$

where $Re = \frac{U_e \delta_r}{\nu_e}$ is a Reynolds number based on characteristic values of edge velocity (U_e), edge kinematic viscosity (ν_e), and reference boundary-layer length scale (δ_r). Thus, PSE considers disturbances of the form

$$\phi' = \int_{-\infty}^{\infty} \underbrace{\tilde{\phi}(\bar{x}, y, \omega)}_{\text{shape}} \underbrace{A(\bar{x}, \omega)e^{-i\omega t}}_{\text{wave}} d\omega \quad (5)$$

where $A(\bar{x}, \omega) = e^i \int \alpha(\bar{x}, \omega) dx$ and the dependence of the shape function ($\tilde{\phi}$) and amplitude function (A) on ω has been made explicit. The shape and amplitude functions are essentially the Fourier transform of the disturbance. Upon expansion of the streamwise derivatives

$$\begin{aligned} \frac{\partial \phi'}{\partial x} &= \int_{-\infty}^{\infty} \left(\frac{1}{Re} \frac{\partial \tilde{\phi}}{\partial \bar{x}} + i\alpha \tilde{\phi} \right) A e^{-i\omega t} d\omega \\ \frac{\partial^2 \phi'}{\partial x^2} &= \int_{-\infty}^{\infty} \left(\frac{1}{Re^2} \frac{\partial^2 \tilde{\phi}}{\partial \bar{x}^2} + \frac{2i\alpha}{Re} \frac{\partial \tilde{\phi}}{\partial \bar{x}} + \frac{i\tilde{\phi}}{Re} \frac{\partial \alpha}{\partial \bar{x}} - \alpha^2 \tilde{\phi} \right) A e^{-i\omega t} d\omega, \end{aligned}$$

it is found that the second spatial derivative $\frac{\partial^2 \tilde{\phi}}{\partial \bar{x}^2}$ is of highest order and a perturbation expansion may be consistently truncated resulting in the neglect of this term. This leaves the disturbance equation nearly parabolized [66], and an efficient marching solution may be sought. JoKHeR implements a wave packet formulation [49, 57] which appears to better represent energy transfer between modes in a nonlinear calculation. Ultimately, in the Quasi-3D formulation, the disturbance is discretely represented as $\phi' = \sum_k \tilde{\phi}(\bar{x}, y)_k A(\bar{x})_k W(\omega)_k e^{-i\omega_k t}$, and a frequency content for each mode is assumed of the form $W_0 = \frac{1}{\sigma_0 \sqrt{2\pi}} e^{-\frac{(\omega - \omega_0)^2}{2\sigma_0^2}}$. With bandwidth of the harmonics obeying $\sigma_t = \sqrt{i+1}\sigma_0$, and harmonic balancing is used to calculate nonlinear interactions. This representation of spectral energy appears to be crucial for modeling the spectral broadening seen in experiments. Note, all perturbation quantities presented in this manuscript are non-dimensionalized in the standard way. Their amplitudes are normalized such that the temperature perturbations maximum amplitude is unity.

4. CHAMPS

The University of Maryland's disturbance flow formulation solves the Nonlinear Disturbance Equations (NLDE) using an over-set mesh approach that attempts to focus computational resources precisely where they are needed most. To this end, the block-structured Cartesian mesh adapts to refine (or coarsen) regions of high (or low) disturbance content. Many details regarding the implementation and validation of this Adaptive Mesh Refinement Wave-packet Tracking (AMR-WPT) solver can be found in Refs. 67 and 68. The disturbance flow derives its energy from the basic state, which is interpolated (high-order) onto the Cartesian mesh. The basic states for each experimental shot were

obtained with the curvilinear framework of CHAMPS, however, those obtained with US3D can be used easily as well. Just quickly, the equations being solved are the NLDE obtained by decomposing the conservative flow state into a known ($\bar{\mathbf{W}}$) basic state and an unknown disturbance state ($\tilde{\mathbf{W}}$).

$$\mathbf{W} = \bar{\mathbf{W}} + \tilde{\mathbf{W}} = \underbrace{\begin{bmatrix} \bar{\rho} \\ \bar{\rho}\bar{u} \\ \bar{\rho}\bar{v} \\ \bar{\rho}\bar{w} \\ \bar{\rho}\bar{E}_t \end{bmatrix}}_{\text{baseflow}} + \underbrace{\begin{bmatrix} \tilde{\rho} \\ \tilde{\rho}\bar{u} + \bar{\rho}\tilde{u} \\ \tilde{\rho}\bar{v} + \bar{\rho}\tilde{v} \\ \tilde{\rho}\bar{w} + \bar{\rho}\tilde{w} \\ \tilde{\rho}\bar{E}_t + \bar{\rho}\tilde{E}_t \end{bmatrix}}_{\text{linear disturbance}} + \underbrace{\begin{bmatrix} 0 \\ \tilde{\rho}\tilde{u} \\ \tilde{\rho}\tilde{v} \\ \tilde{\rho}\tilde{w} \\ \tilde{\rho}\tilde{E}_t \end{bmatrix}}_{\text{nonlinear disturbance}}. \quad (6)$$

In the derivation of the disturbance flow equations, the total fluxes are also decomposed in the form

$$\mathbf{E} = \bar{\mathbf{E}} + \tilde{\mathbf{E}}, \quad \mathbf{F} = \bar{\mathbf{F}} + \tilde{\mathbf{F}}, \quad \text{and} \quad \mathbf{G} = \bar{\mathbf{G}} + \tilde{\mathbf{G}}, \quad (7)$$

where, for example, the convective and viscous components of the flux in the x-direction, \mathbf{E} , can be written as

$$\mathbf{E}_c = \underbrace{\begin{bmatrix} \bar{\rho}\bar{u} \\ \bar{\rho}\bar{u}^2 + \bar{p} \\ \bar{\rho}\bar{u}\bar{v} \\ \bar{\rho}\bar{u}\bar{w} \\ (\bar{\rho}\bar{E}_t + \bar{p})\bar{u} \end{bmatrix}}_{\text{baseflow}} + \underbrace{\begin{bmatrix} \tilde{\rho}\bar{u} + \bar{\rho}\tilde{u} \\ \tilde{\rho}\bar{u}^2 + 2\bar{\rho}\bar{u}\tilde{u} + \bar{p} \\ \tilde{\rho}\bar{u}\bar{v} + \bar{\rho}\bar{u}\tilde{v} + \bar{\rho}\tilde{u}\bar{v} \\ \tilde{\rho}\bar{u}\bar{w} + \bar{\rho}\bar{u}\tilde{w} + \bar{\rho}\tilde{u}\bar{w} \\ (\tilde{\rho}\bar{E}_t + \bar{\rho}\tilde{E}_t + \bar{p})\bar{u} + (\bar{\rho}\bar{E}_t + \bar{p})\tilde{u} \end{bmatrix}}_{\text{linear disturbance}} + \underbrace{\begin{bmatrix} \tilde{\rho}\tilde{u} \\ \tilde{\rho}\bar{u}^2 + \bar{\rho}\tilde{u}^2 + 2\bar{\rho}\bar{u}\tilde{u} \\ \tilde{\rho}\bar{u}\tilde{v} + \bar{\rho}\tilde{u}\bar{v} + \bar{\rho}\tilde{u}\tilde{v} + \bar{\rho}\tilde{u}\bar{v} \\ \tilde{\rho}\bar{u}\tilde{w} + \bar{\rho}\tilde{u}\bar{w} + \bar{\rho}\tilde{u}\tilde{w} + \bar{\rho}\tilde{u}\bar{w} \\ (\tilde{\rho}\bar{E}_t + \bar{\rho}\tilde{E}_t + \bar{\rho}\tilde{E}_t + \bar{p})\bar{u} + \bar{\rho}\tilde{E}_t\tilde{u} \end{bmatrix}}_{\text{nonlinear disturbance}}, \quad \text{and}$$

$$\mathbf{E}_v = - \underbrace{\begin{bmatrix} 0 \\ \bar{\mu}\bar{\tau}_{xx} \\ \bar{\mu}\bar{\tau}_{xy} \\ \bar{\mu}\bar{\tau}_{xz} \\ \bar{\mathcal{E}} \end{bmatrix}}_{\text{baseflow}} - \underbrace{\begin{bmatrix} 0 \\ \bar{\mu}\bar{\tau}_{xx} + \tilde{\mu}\bar{\tau}_{xx} \\ \bar{\mu}\bar{\tau}_{xy} + \tilde{\mu}\bar{\tau}_{xy} \\ \bar{\mu}\bar{\tau}_{xz} + \tilde{\mu}\bar{\tau}_{xz} \\ \tilde{\mathcal{E}}_l \end{bmatrix}}_{\text{linear disturbance}} - \underbrace{\begin{bmatrix} 0 \\ \tilde{\mu}\bar{\tau}_{xx} \\ \tilde{\mu}\bar{\tau}_{xy} \\ \tilde{\mu}\bar{\tau}_{xz} \\ \tilde{\mathcal{E}}_{nl} \end{bmatrix}}_{\text{nonlinear disturbance}}. \quad (8)$$

The energy flux components of the viscous flux in Eq. (8) are expressed as

$$\bar{\mathcal{E}} = -\bar{\mu} (\bar{u}\bar{\tau}_{xx} + \bar{v}\bar{\tau}_{xy} + \bar{w}\bar{\tau}_{xz}) - \bar{k} \frac{\partial \bar{T}}{\partial x}, \quad (9)$$

$$\tilde{\mathcal{E}}_l = -\bar{\mu} (\bar{u}\bar{\tau}_{xx} + \tilde{u}\bar{\tau}_{xx} + \bar{v}\bar{\tau}_{xy} + \tilde{v}\bar{\tau}_{xy} + \bar{w}\bar{\tau}_{xz} + \tilde{w}\bar{\tau}_{xz}) - \bar{\mu} (\bar{u}\bar{\tau}_{xx} + \bar{v}\bar{\tau}_{xy} + \bar{w}\bar{\tau}_{xz}) - \bar{k} \frac{\partial \bar{T}}{\partial x} - \tilde{k} \frac{\partial \bar{T}}{\partial x}, \quad \text{and} \quad (10)$$

$$\tilde{\mathcal{E}}_{nl} = -\bar{\mu} (\tilde{u}\bar{\tau}_{xx} + \tilde{v}\bar{\tau}_{xy} + \tilde{w}\bar{\tau}_{xz}) - \bar{\mu} (\tilde{u}\bar{\tau}_{xx} + \tilde{u}\bar{\tau}_{xx} + \tilde{u}\bar{\tau}_{xx} + \bar{v}\bar{\tau}_{xy} + \tilde{v}\bar{\tau}_{xy} + \tilde{v}\bar{\tau}_{xy} + \bar{w}\bar{\tau}_{xz} + \tilde{w}\bar{\tau}_{xz} + \tilde{w}\bar{\tau}_{xz}) - \tilde{k} \frac{\partial \bar{T}}{\partial x}. \quad (11)$$

After eliminating the pure baseflow contribution on the right-hand-side of the governing equations assuming the baseflow has been adequately converged to a steady-state solution (see Ref. 69 for more details) the final form of the nonlinear disturbance equations can be cast in the form

$$\frac{\partial \tilde{\mathbf{W}}}{\partial t} + \frac{\partial \tilde{\mathbf{E}}}{\partial x} + \frac{\partial \tilde{\mathbf{F}}}{\partial y} + \frac{\partial \tilde{\mathbf{G}}}{\partial z} = 0, \quad (12)$$

where the total flux vectors $\tilde{\mathbf{E}}$, $\tilde{\mathbf{F}}$ and $\tilde{\mathbf{G}}$ are a function of $\tilde{\mathbf{W}}$ and $\tilde{\mathbf{W}}$ and its gradients, as can be seen in Eqs. (6)-(11). At the moment, the main ability for incorporating real gas effects in the NLDE simulations performed with CHAMPS is through interpolation of the transport properties of the precomputed basic state onto the disturbance mesh. For better comparison between the computational results, the calculations were performed without the nonlinear terms and, thus, solved the linearized disturbance equations.

IV. Results

A. Experimental

We begin by presenting experimental results for the previously discussed experiments performed at T5. Shot 2990 represented an experiment with a transitional boundary layer at relatively high enthalpy (8.9 MJ/kg) during which the cone's surface was not actively cooled. The averaged power spectral density (PSD) for this experiment is shown in Fig. 4a. The upstream and downstream probes within the boundary layer show distinct peaks representing the second-mode instability at approximately $f_{2M} = 1250$ kHz. Elevated low-frequency spectral content is observed by the probes outside of the boundary layer. To further investigate a second-mode wave packet observed during the test time, we perform a short-time Fourier transform centered in time around the emergence of the instability. The resulting short-time PSD is presented in Fig. 4b. Here, in addition to the second-mode instability being measured by the FLDI probes positioned inside the boundary layer, the first harmonic of the instability is observed at approximately 2600 kHz. Higher-order spectral analysis was used to verify the presence of quadratic phase-coupled interactions generating the harmonic through nonlinear processes [38, 70].

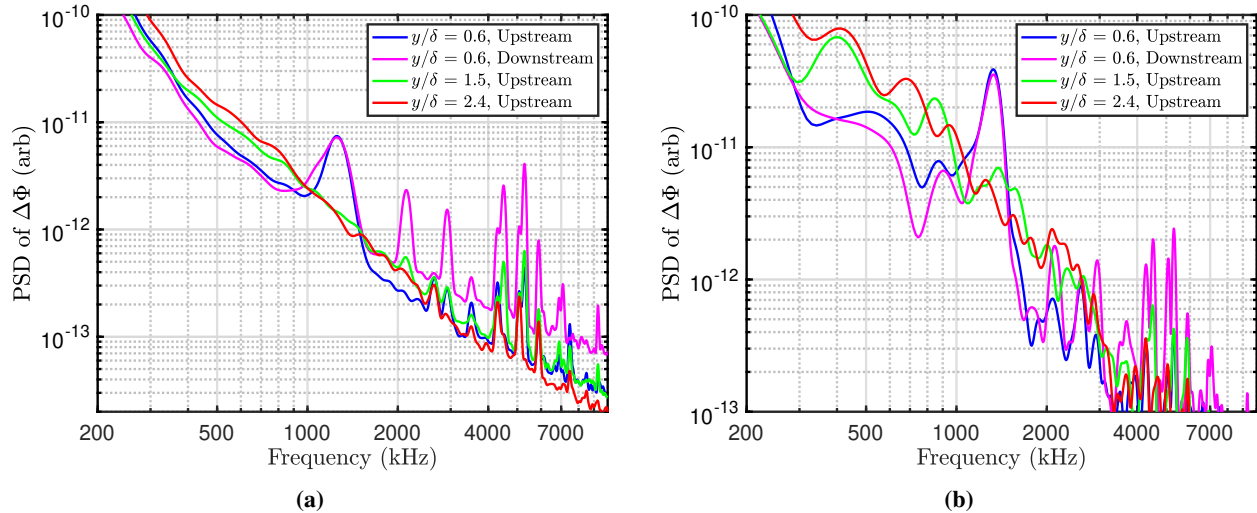


Fig. 4 (a) Averaged PSD for shot 2990. The second-mode instability is observed by the upstream and downstream probes located within the boundary layer. (b) Short-time PSD for shot 2990. The first harmonic of the second-mode instability is observed at approximately 2600 kHz in the spectra of the FLDI probes located within the boundary layer.

The averaged PSDs for shots 3022 and 3026 are presented in Fig. 5. These experiments were performed with an actively-cooled cone- the wall-temperature profile along the cone for each experiment is provided in Table 3. For both experiments, the second-mode instability was observed by the FLDI probes located within the boundary layer, however, its amplitude was comparatively lower than that measured in shot 2990. Interestingly, the measured frequency of the second-mode instability for shots 3022 and 3026 agreed fairly well with the frequency measured for shot 2990. For shot 3022, the measured frequency of the second-mode instability was approximately 1280 kHz for the upstream probe and 1240 kHz for the downstream probe. For shot 3026, the measured frequency of the second-mode instability was approximately 1250 kHz and 1150 kHz for the upstream and downstream probes within the boundary layer. We note that the second-mode peaks observed in shot 3026 were broader for both FLDI probes than those observed in shots 2990 and 3022. Although no clear harmonics were observed in these averaged PSDs, early quadratic phase coupling between

the second mode and its harmonic may not be visible [71]; higher-order spectral analysis is necessary to conclusively determine the presence of nonlinear interactions for these experiments.

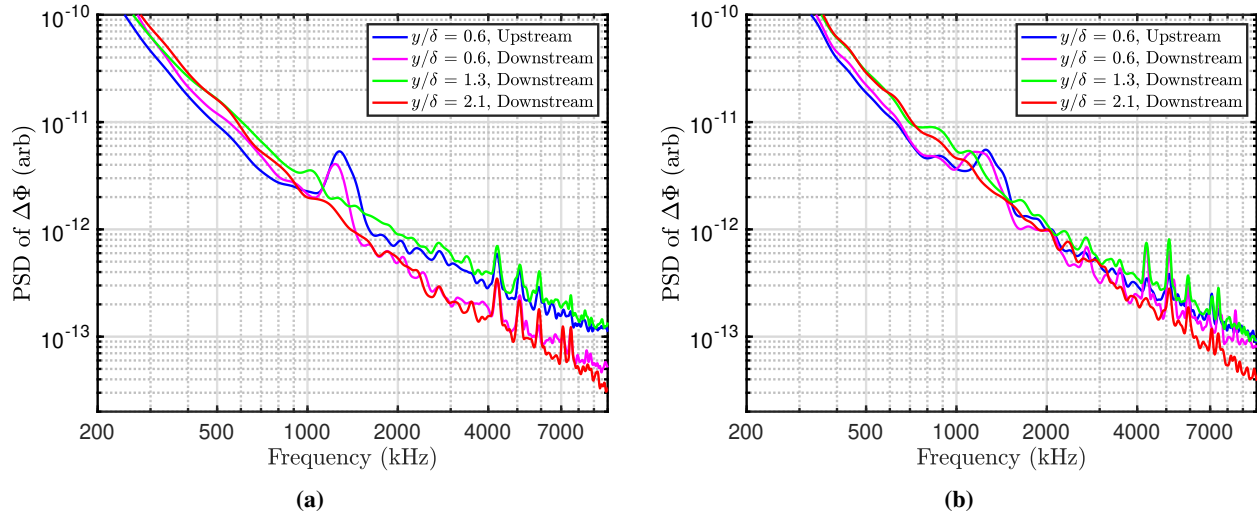


Fig. 5 Averaged PSD for (a) shot 3022 and (b) shot 3026. The second-mode instability is observed by the upstream and downstream probes within the boundary layer, however, it is appreciably weaker than shot 2990.

B. Numerical

Numerical calculations from ONERA’s MAMOUT (LST code with real gas effects), University of Delaware’s JoKHeR (LPSE code with ideal gas effects), Steven’s Institute of Technology’s version of the STABL (LPSE code with real gas effects) and University of Maryland’s CHAMPS (NLDE code with real gas effects) codes were compared with experimental results. Each numerical group was given the run conditions and geometry of interest and asked to calculate the boundary-layer instabilities. The goal of this comparison was to begin understanding the range of predictability using different stability approaches for high-enthalpy flows. N-factors were extracted from each numerical calculation at the point corresponding to the experimental data collection site. The comparison results can be seen in Fig. 6.

Several overall trends are common for each of the four shots considered.

- 1) The LST and LPSE based solvers tend to identify peak instability at higher frequencies ($\approx 1500\text{-}1600\text{kHz}$) than those observed experimentally.
- 2) The NLDE based solver (closer to a direct numerical simulation approach) consistently predicts peak instability frequencies accurately when compared to the experiments. However, a lower amplified tail in the spectrum is observed into the range seen by the LST and PSE codes.
- 3) The calculated disturbance amplitude for the JoKHeR LPSE and NLDE did not show sensitivity to wall temperature (shot 2990, versus 30–40K colder cases 3019, 3022, 3026). Note that these two solvers make the ideal gas assumption. However, the LST, and to a lesser extent STABL LPSE, results using real gas effects did exhibit sensitivity to wall temperature.
- 4) The JoKHeR LPSE code was run with isothermal and adiabatic boundary conditions for the temperature disturbance. It is interesting to note the sensitivity of the disturbance amplitude to this boundary condition. Also, notice that the real gas LST and NLDE results seem to be somewhat bracketed by the choice of boundary condition.
- 5) In general, the two LPSE solvers found similar disturbance amplification. While the real gas LST and ideal gas NLDE, tended to predict similar disturbance amplitudes.

Ultimately, the amount of spread in the prediction is somewhat surprising, when compared to similar studies conducted in low-enthalpy quiet tunnels [53]. Concerning the frequency prediction, it is fairly well-established that the second-mode frequency is tied closely to the boundary layer length scale, in the sense of the thermoacoustic resonance mechanism. However, for high-enthalpy flows, the boundary layer height is affected by finite-rate chemistry dynamics. It is curious to note that the best numerical prediction, in terms of most unstable frequency, we achieved by the only code which did not utilize real gas effects for the basic state calculation. Future efforts to better reign in such uncertainty

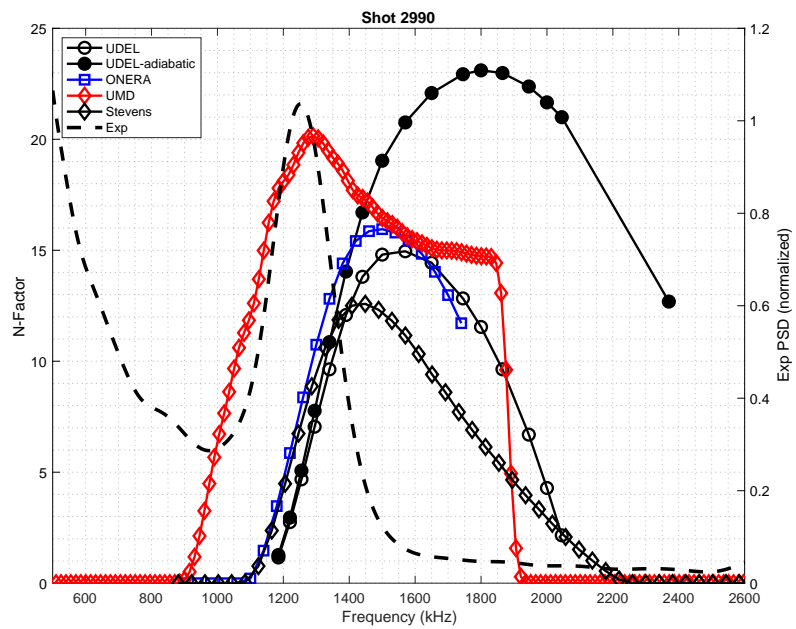
should consider detailed comparisons of basic state profiles and specific treatment of real gas effects.

In terms of amplitude prediction, there is also significant uncertainty. The two LPSE codes predicted similar disturbance amplification (N-factors around 13-15), while the NLDE and real gas LST both predicted similar disturbance amplification factors (N-factors around 20). However, an N-factor difference of 5 is a very significant spread. It should be noted, that bicoherence analysis of experimental shot 2990 indicates the presence of harmonics. While the boundary layers did not appear to be transitions, nonlinearity may play a role in this discrepancy. Also, LPSE cases with adiabatic disturbance boundary conditions were considered. It is interesting to note that while the adiabatic boundary condition negatively affects the most unstable frequency prediction, it may be able to account for the discrepancy in amplification prediction. Future work should more thoroughly study the influence of nonlinearity and thermal boundary conditions on high-enthalpy stability and transition prediction.

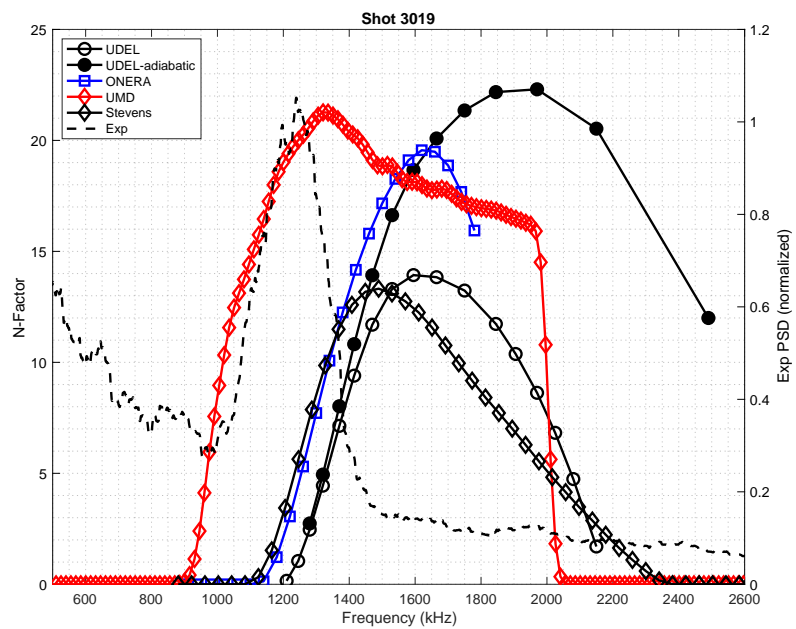
V. Conclusions

Experimental results gathered at Caltech's T5 free piston reflected shock tunnel were compared with N factor calculations performed using various numerical stability solvers. The LST and LPSE based solvers (ONERA's MAMOUT, University of Delaware's JoKHeR, and STABL) identified peak second-mode instability at a higher frequency than the experimental observation. The NLDE based CHAMPS solver from the University of Maryland was more accurate in predicting the second-mode frequency. Some of the experiments were performed with an actively-cooled wall (30-40 K colder). A comparison of the numerical results for these experiments to shot 2990, which was performed with an isothermal wall, shows that MAMOUT and (to a lesser extent) STABL (both solvers using real gas effects), were sensitive to wall temperature, while the JoKHeR and CHAMPS solvers did not exhibit such sensitivity. The N factor amplitudes computed by JoKHeR and STABL agreed fairly well with each other, and amplitudes observed amongst the real gas LST and ideal gas NLDE solvers were also in good agreement.

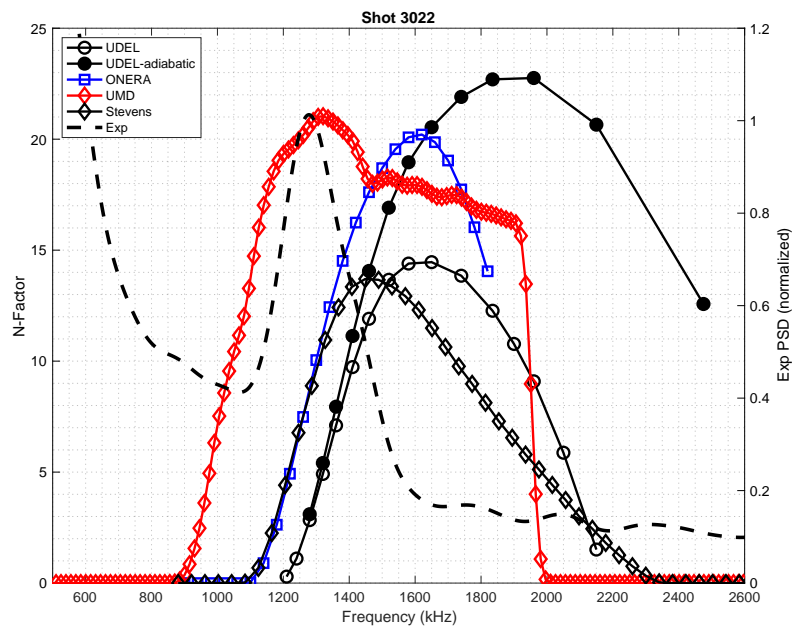
There was significant uncertainty observed in both N factor maximum amplitude and the most amplified frequency. Interestingly, the NLDE solver (only code not utilizing real gas effects), provided the best agreement in terms of frequency. Although the predicted disturbance amplification factors were similar between the two LPSE solvers as well as the NLDE and real gas LST solvers, there was an N-factor difference of 5 between these two sets. This significant discrepancy could be partially explained by nonlinearity observed in the experimental data of shot 2990 as well as proper specification of the thermal boundary condition.



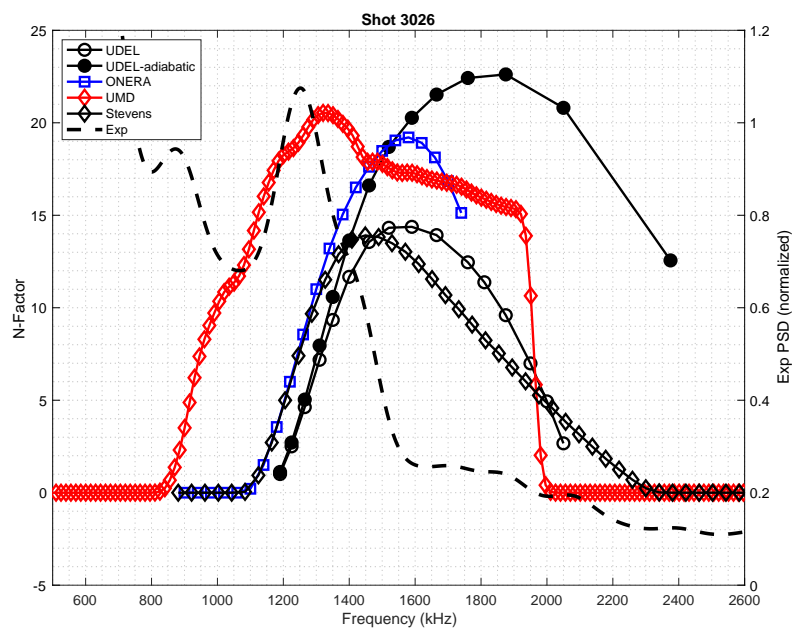
(a)



(b)



(c)



(d)

Fig. 6 Comparison between experimental and numerical results for shots (a) 2990, (b) 3019, (c) 3022, and (d) 3026. Experimental PSDs are normalized by the peak amplitude of the second-mode instability in each experiment.

References

- [1] Schneider, S. P., "Flight data for boundary-layer transition at hypersonic and supersonic speed," *Journal of Spacecraft and Rockets*, Vol. 36, No. 1, 1999, pp. 8–20. <https://doi.org/10.2514/2.3428>.
- [2] MacLean, M., Wadhams, T., Holden, M., and Johnson, H., "Ground test studies of the HIFiRE-1 transition experiment Part 2: computational analysis," *Journal of Spacecraft and Rockets*, Vol. 45, No. 6, 2008, pp. 1149–1164. <https://doi.org/10.2514/1.37693>.
- [3] DSB, "Report of the Defense Science Board Task Force on the National Aerospace Plane (NASP)," AD-A201 124, 1988.
- [4] Sherman, M., and Nakamura, T., "Flight test measurements of boundary-layer transition on a nonablating 22 deg cone," *Journal of Spacecraft and Rockets*, Vol. 7, No. 2, 1970, pp. 137–142. <https://doi.org/10.2514/3.29888>.
- [5] Malik, M. R., "Hypersonic Flight Transition Data Analysis Using Parabolized Stability Equations with Chemistry Effects," *Journal of Spacecraft and Rockets*, Vol. 40, No. 3, 2003, pp. 332–344. <https://doi.org/10.2514/2.3968>.
- [6] Lees, L., "The Stability of the Laminar Boundary Layer in a Compressible Fluid," NASA-TN, 1947.
- [7] Mack, L. M., "Review of Linear Compressible Stability Theory," *Stability of Time Dependent and Spatially Varying Flows: Proceedings of the Symposium on the Stability of Time Dependent and Spatially Varying Flows*, Springer-Verlag, Hampton, Virginia, 1987. https://doi.org/10.1007/978-1-4612-4724-1_9.
- [8] Mack, L., "Effect of Cooling on Boundary-Layer Stability at Mach Number 3," *Instabilities and Turbulence in Engineering Flows*, Springer, 1993, pp. 175–188. https://doi.org/10.1007/978-94-011-1743-2_9.
- [9] Bitter, N. P., and Shepherd, J. E., "Stability of highly cooled hypervelocity boundary layers," *Journal of Fluid Mechanics*, Vol. 778, No. 10, 2015, pp. 586–620. <https://doi.org/10.1017/jfm.2015.358>.
- [10] Knisely, C. P., and Zhong, X., "Sound radiation by supersonic unstable modes in hypersonic blunt cone boundary layers. I. Linear stability theory," *Physics of Fluids*, Vol. 31, No. 2, 2019, p. 024103. <https://doi.org/10.1063/1.5055761>.
- [11] Knisely, C. P., and Zhong, X., "Sound radiation by supersonic unstable modes in hypersonic blunt cone boundary layers. II. Direct numerical simulation," *Physics of Fluids*, Vol. 31, No. 2, 2019, p. 024104. <https://doi.org/10.1063/1.5077007>.
- [12] Chuvakhov, P. V., and Fedorov, A. V., "Spontaneous radiation of sound by instability of a highly cooled hypersonic boundary layer," *Journal of Fluid Mechanics*, Vol. 805, 2016, pp. 188–206. <https://doi.org/10.1017/jfm.2016.560>.
- [13] Unnikrishnan, S., and Gaitonde, D. V., "Instabilities and transition in cooled wall hypersonic boundary layers," *Journal of Fluid Mechanics*, Vol. 915, 2021, p. A26. <https://doi.org/10.1017/jfm.2021.84>.
- [14] Chang, C. L., Vinh, H., and Malik, M., "Hypersonic boundary-layer stability with chemical reactions using PSE," *28th Fluid Dynamics Conference*, AIAA-97-2012, Snowmass Village, CO, 1997. <https://doi.org/10.2514/6.1997-2012>.
- [15] Johnson, H. B., Seipp, T. G., and Candler, G. V., "Numerical Study of Hypersonic Reacting Boundary Layer Transition on Cones," *Physics of Fluids*, Vol. 10, No. 13, 1998, pp. 2676–2685. <https://doi.org/10.1063/1.869781>.
- [16] Adam, P. H., and Hornung, H. G., "Enthalpy Effects on Hypervelocity Boundary-layer Transition: Ground Test and Flight Data," *Journal of Spacecraft And Rockets*, Vol. 34, No. 5, 1997, pp. 614–619. <https://doi.org/10.2514/2.3278>.
- [17] Germain, P. D., and Hornung, H. G., "Transition on a Slender Cone in Hypervelocity Flow," *Experiments in Fluids*, Vol. 22, 1997, pp. 183–190. <https://doi.org/10.1007/s003480050036>.
- [18] Vidal, R., and Golian, T., "Heat-Transfer Measurements with a Catalytic Flat Plate in Dissociated Oxygen," *AIAA Journal*, Vol. 5, No. 9, 1967, pp. 1579–1588. <https://doi.org/10.2514/3.4254>.
- [19] East, R., Stalker, R., and Baird, J., "Measurements of heat transfer to a flat plate in a dissociated high-enthalpy laminar air flow," *Journal of Fluid Mechanics*, Vol. 97, No. 4, 1980, pp. 673–699. <https://doi.org/10.1017/S0022112080002753>.
- [20] Germain, P., "The Boundary Layer On a Sharp Cone in High-enthalpy Flow," Ph.D. thesis, California Institute of Technology, California, 1993.
- [21] Adam, P., "Enthalpy Effects on Hypervelocity Boundary Layers," Ph.D. thesis, California Institute of Technology, California, 1997.

- [22] Rasheed, A., "Passive Hypervelocity Boundary Layer Control Using an Acoustically Absorptive Surface," Ph.D. thesis, California Institute of Technology, California, 2001.
- [23] Rasheed, A., Hornung, H. G., Fedorov, A. V., and Malmuth, N. D., "Experiments on Passive Hypervelocity Boundary-layer Control Using an Ultrasonically Absorptive Surface," *AIAA J.*, Vol. 40, No. 3, 2002, pp. 481–489. <https://doi.org/10.2514/2.1671>.
- [24] Fujii, K., and Hornung, H. G., "A Procedure to Estimate the Absorption Rate of Sound Propagating Through High Temperature Gas," GALCIT Report FM 2001.004, 2001.
- [25] Leyva, I., Laurence, S., Beierholm, A. K., Hornung, H., Wagnild, R., and Candler, G., "Transition Delay in Hypervelocity Boundary Layers by Means of CO₂/Acoustic Instability Interactions," *Proceedings of 47th AIAA Aerospace Sciences Meeting Including the New Horizons Forum and Aerospace Exposition*, AIAA-2009-1287, Orlando, Florida, 2009. <https://doi.org/10.2514/6.2009-1287>.
- [26] Leyva, I., Laurence, S., Beierholm, A. K., Hornung, H., Wagnild, R., and Candler, G., "On the Impact of Injection Schemes on Transition in Hypersonic Boundary Layers," *Proceedings of 16th AIAA/DLR/DGLR International Space Planes and Hypersonic Systems and Technologies Conference*, AIAA-2009-7204, Bremen, Germany, 2009. <https://doi.org/10.2514/6.2009-7204>.
- [27] Jewell, J. S., Leyva, I. A., Parziale, N. J., and Shepherd, J. E., "Effect of Gas Injection on Transition in Hypervelocity Boundary Layers," *Proceedings of the 28th International Symposium on Shock Waves*, ISSW-2767, Manchester, UK, 2011, pp. 735–740. https://doi.org/10.1007/978-3-642-25688-2_111.
- [28] Jewell, J. S., Parziale, N. J., Leyva, I. A., Shepherd, J. E., and Hornung, H. G., "Turbulent Spot Observations within a Hypervelocity Boundary Layer on a 5-degree Half-Angle Cone," *Proceedings of 42nd AIAA Fluid Dynamics Conference and Exhibit*, AIAA-2012-3062, New Orleans, Louisiana, 2012. <https://doi.org/10.2514/6.2012-3062>.
- [29] Jewell, J. S., Wagnild, R. M., Leyva, I. A., Candler, G. V., and Shepherd, J. E., "Transition Within a Hypervelocity Boundary Layer on a 5-Degree Half-Angle Cone in Air/CO₂ Mixtures," *Proceedings of 51st AIAA Aerospace Sciences Meeting including the New Horizons Forum and Aerospace Exposition*, AIAA-2013-0523, Grapevine, Texas, 2013. <https://doi.org/10.2514/6.2013-523>.
- [30] Parziale, N. J., Jewell, J. S., Shepherd, J. E., and Hornung, H. G., "Optical Detection of Transitional Phenomena on Slender Bodies in Hypervelocity Flow," *Proceedings of RTO Specialists Meeting AVT-200/RSM-030 on Hypersonic Laminar-Turbulent Transition*, NATO, San Diego, California, 2012.
- [31] Parziale, N. J., Shepherd, J. E., and Hornung, H. G., "Differential Interferometric Measurement of Instability at Two Points in a Hypervelocity Boundary Layer," *Proceedings of 51st AIAA Aerospace Sciences Meeting Including the New Horizons Forum and Aerospace Exposition*, AIAA-2013-0521, Grapevine, Texas, 2013. <https://doi.org/10.2514/6.2013-521>.
- [32] Parziale, N. J., Shepherd, J. E., and Hornung, H. G., "Differential Interferometric Measurement of Instability in a Hypervelocity Boundary Layer," *AIAA Journal*, Vol. 51, No. 3, 2013, pp. 750–753. <https://doi.org/10.2514/1.J052013>.
- [33] Parziale, N. J., "Slender-Body Hypervelocity Boundary-Layer Instability," Ph.D. thesis, California Institute of Technology, 2013.
- [34] Tanno, H., Komura, T., Sato, K., Itoh, K., Takahashi, M., and Fujii, K., "Measurements of Hypersonic Boundary Layer Transition on Cone Models in the Free-Piston Shock Tunnel HIEST," *Proceedings of 47th AIAA Aerospace Sciences Meeting including The New Horizons Forum and Aerospace Exposition*, AIAA, Orlando, FL, 2009.
- [35] Tanno, H., Komuro, T., Sato, K., Itoh, K., Takahashi, M., and Fujii, K., "Measurement of hypersonic high-enthalpy boundary layer transition on a 7° cone model," *48th AIAA Aerospace Sciences Meeting Including the New Horizons Forum and Aerospace Exposition*, AIAA, Orlando, FL, 2010. <https://doi.org/10.2514/6.2010-310>.
- [36] Laurence, S. J., Wagner, A., and Hannemann, K., "Experimental study of second-mode instability growth and breakdown in a hypersonic boundary layer using high-speed schlieren visualization," *Journal of Fluid Mechanics*, Vol. 797, 2016, pp. 471–503. <https://doi.org/10.1017/jfm.2016.280>.
- [37] Hameed, A., Shekhtman, D., Parziale, N. J., Paquin, L. A., Skinner, S., Laurence, S. J., Yu, W. M., and Austin, J. M., "Hypersonic Boundary-Layer Instability on a Highly Cooled Cone. Part I: Q-FLDI Measurement and Instability Calculations," *Proceedings of AIAA Scitech 2022*, AIAA-2022-0734, San Diego, California and Virtual Event, 2022. <https://doi.org/10.2514/6.2022-0734>.
- [38] Hameed, A., Parziale, N. J., Paquin, L. A., Laurence, S. J., Yu, W. M., and Austin, J. M., "Characterization of Transitional, High-Enthalpy Boundary Layers on a Blunted Cone. Part II: FLDI and Higher Order Spectral Analysis," *Proceedings of AIAA Scitech 2023*, AIAA-2023-0288, National Harbor, Maryland and Virtual Event, 2023. <https://doi.org/10.2514/6.2023-0288>.

- [39] Paquin, L. A., Laurence, S. J., Hameed, A., Parziale, N. J., Yu, W. M., and Austin, J. M., "Characterization of Transitional, High-Enthalpy Boundary Layers on a Slightly-Blunted Cone. Part I: Schlieren Imaging," *Proceedings of AIAA Scitech 2023*, Submitted.
- [40] Hornung, H. G., "Performance Data of the New Free-Piston Shock Tunnel at GALCIT," *Proceedings of 17th AIAA Aerospace Ground Testing Conference*, AIAA 1992-3943, Nashville, TN, 1992. <https://doi.org/10.2514/6.1992-3943>.
- [41] Goodwin, D. G., "An Open-Source, Extensible Software Suite for CVD Process Simulation," *Proceedings of CVD XVI and EuroCVD Fourteen*, M Allendorf, F Maury, and F Teysandier (Eds.), 2003, pp. 155–162.
- [42] Browne, S., Ziegler, J., and Shepherd, J. E., "Numerical Solution Methods for Shock and Detonation Jump Conditions," GALCIT - FM2006-006, Caltech, 2006.
- [43] Wright, M. J., Candler, G. V., and Prampolini, M., "Data-parallel Lower-upper Relaxation Method for the Navier-Stokes Equations," *AIAA Journal*, Vol. 34, No. 7, 1996, pp. 1371–1377. <https://doi.org/10.2514/3.13242>.
- [44] Candler, G. V., "Hypersonic Nozzle Analysis Using an Excluded Volume Equation of State," *Proceedings of 38th AIAA Thermophysics Conference*, AIAA-2005-5202, Toronto, Ontario Canada, 2005. <https://doi.org/10.2514/6.2005-5202>.
- [45] Johnson, H. B., "Thermochemical Interactions in Hypersonic Boundary Layer Stability," Ph.D. thesis, University of Minnesota, Minneapolis, Minnesota, 2000.
- [46] Wagnild, R. M., "High Enthalpy Effects on Two Boundary Layer Disturbances in Supersonic and Hypersonic Flow," Ph.D. thesis, University of Minnesota, Minnesota, 2012.
- [47] Paquin, L. A., Skinner, S. N., Laurence, S. J., Hameed, A., Shekhtman, D., Parziale, N. J., Yu, W. M., and Austin, J. M., "Hypersonic Boundary-Layer Instability on a Highly Cooled Cone. Part II: Schlieren Analysis of Boundary-Layer Disturbances," *Proceedings of AIAA Scitech 2022*, AIAA-2022-0947, San Diego, California and Virtual Event, 2022. <https://doi.org/10.2514/6.2022-0947>.
- [48] Kuehl, J. J., Perez, E., and Reed, H. L., "JoKHeR: NPSE Simulations of Hypersonic Cross Instability," *AIAA Aerospace Science Meeting*, Vol. 921, 2012.
- [49] Kuehl, J. J., "Discrete-and finite-bandwidth-frequency distributions in nonlinear stability applications," *Physics of Fluids*, Vol. 29, No. 2, 2017.
- [50] Perez, E., Reed, H. L., and Kuehl, J., "Instabilities on a hypersonic yawed straight cone," *43rd AIAA Fluid Dynamics Conference*, 2013, p. 2879.
- [51] Hofferth, J., Saric, W., Kuehl, J., Perez, E., Kocian, T., and Reed, H., "Boundary-layer instability and transition on a flared cone in a Mach 6 quiet wind tunnel," *International Journal of Engineering Systems Modelling and Simulation* 47, Vol. 5, No. 1-3, 2013, pp. 109–124.
- [52] Kocian, T., Perez, E., Oliviero, N., Kuehl, J., and Reed, H., "Hypersonic stability analysis of a flared cone," *51st AIAA Aerospace Sciences Meeting Including the New Horizons Forum and Aerospace Exposition*, 2013, p. 667.
- [53] Chynoweth, B. C., Schneider, S. P., Hader, C., Fasel, H., Batista, A., Kuehl, J., Juliano, T. J., and Wheaton, B. M., "History and progress of boundary-layer transition on a Mach-6 flared cone," *Journal of Spacecraft and Rockets*, Vol. 56, No. 2, 2019, pp. 333–346.
- [54] Reed, H. L., Perez, E., Kuehl, J., Kocian, T., and Oliviero, N., "Verification and validation issues in hypersonic stability and transition prediction," *Journal of Spacecraft and Rockets*, Vol. 52, No. 1, 2015, pp. 29–37.
- [55] Kuehl, J., and Paredes, P., "Gortler modified mack-modes on a hypersonic flared cone," *54th AIAA Aerospace Sciences Meeting*, 2016, p. 0849.
- [56] Perez, E., Kocian, T., Kuehl, J., and Reed, H., "Stability of hypersonic compression cones," *42nd AIAA Fluid Dynamics Conference and Exhibit*, 2012, p. 2962.
- [57] Kuehl, J., Reed, H. L., Kocian, T., and Oliviero, N., "Bandwidth effects on Mack-mode instability," *7th AIAA Theoretical Fluid Mechanics Conference*, 2014, p. 2777.
- [58] Batista, A., and Kuehl, J., "A mechanism for spectral broadening and implications for saturation amplitude estimates," *47th AIAA Fluid Dynamics Conference*, 2017, p. 3635.

- [59] Kuehl, J., “Nonlinear saturation versus nonlinear detuning: Quantification on a Mach 6 flared cone,” *55th AIAA Aerospace Sciences Meeting*, 2017, p. 0763.
- [60] Wright, M. J., Candler, G. V., and Bose, D., “Data-Parallel Line Relaxation Method for the Navier-Stokes Equations,” *AIAA Journal*, Vol. 36, No. 9, 1998, pp. 1603–1609. <https://doi.org/10.2514/2.586>.
- [61] Johnson, H. B., and Candler, G., “Hypersonic boundary layer stability analysis using PSE-Chem,” *35th AIAA fluid dynamics conference and exhibit*, IEEE, Toronto, Ontario, Canada, 2005, p. 5023. <https://doi.org/10.2514/6.2005-5023>.
- [62] Herbert, T., and Bertolotti, F., “Stability analysis of nonparallel boundary layers,” *Bull. Am. Phys. Soc.*, Vol. 32, No. 2079, 1987, p. 590.
- [63] Gaster, M., “On the effects of boundary-layer growth on flow stability,” *Journal of Fluid Mechanics*, Vol. 66, No. 3, 1974, pp. 465–480.
- [64] Herbert, T., “Parabolized stability equations,” *Annual Review of Fluid Mechanics*, Vol. 29, No. 1, 1997, pp. 245–283.
- [65] Chang, C.-L., Malik, M., Erlebacher, G., and Hussaini, M., “Compressible stability of growing boundary layers using parabolized stability equations,” *22nd Fluid Dynamics, Plasma Dynamics and Lasers Conference*, 1991, p. 1636.
- [66] Li, F., and Malik, M. R., “On the nature of PSE approximation,” *Theoretical and Computational Fluid Dynamics*, Vol. 8, No. 4, 1996, pp. 253–273.
- [67] Browne, O. M. F., Haas, A. P., Fasel, H. F., and Brehm, C., “An efficient linear wavepacket tracking method for hypersonic boundary-layer stability prediction,” *J. Comput. Phys.*, Vol. 380, 2019, pp. 243–268.
- [68] Browne, O. M. F., Haas, A. P., Fasel, H. F., and Brehm, C., “An Efficient Strategy for Computing Wave-Packets in High-Speed Boundary Layers,” *47th AIAA Fluid Dynamics Conference, Denver, CO*, 2017.
- [69] Browne, O. M., Haas, A. P., Fasel, H. F., and Brehm, C., “A nonlinear compressible flow disturbance formulation for adaptive mesh refinement wavepacket tracking in hypersonic boundary-layer flows,” *Computers & Fluids*, Vol. 240, 2022, p. 105395. <https://doi.org/https://doi.org/10.1016/j.compfluid.2022.105395>, URL <https://www.sciencedirect.com/science/article/pii/S0045793022000652>.
- [70] Hameed, A., “Spectral Analysis of Hypersonic Boundary-Layer Instability,” Ph.D. thesis, Stevens Institute of Technology, 2023.
- [71] Craig, S. A., Humble, R. A., Hofferth, J. W., and Saric, W. S., “Nonlinear behaviour of the Mack mode in a hypersonic boundary layer,” *Journal of Fluid Mechanics*, Vol. 872, 2019, pp. 74–99. <https://doi.org/10.1017/jfm.2019.359>.